AIAA JOURNAL
Vol. 40, No. 7, July 2002

Navier–Stokes Analysis of Wind-Tunnel Interference on Transonic Airfoil Flutter

B. M. Castro*
Naval Postgraduate School, Monterey, California 93943
J. A. Ekaterinaris†
Foundation for Research and Technology Hellas, 71110 Heraklion, Greece
and
M. F. Platzer‡
Naval Postgraduate School, Monterey, California 93943

A time-domain numerical method is used for the simulation and investigation of the transonic two-degree-of-freedom bending/torsion flutter characteristics of the National Aerospace Laboratory 7301 section measured in a wind-tunnel experiment. An implicit, time-accurate, two-dimensional, compressible, thin-layer Navier–Stokes flow solver is coupled with a two-degree-of-freedom structural model. The wind-tunnel walls are included to model the experimental flow conditions more closely and to obtain accurate aerodynamic predictions in the computations. A three-block grid is used for the discretization of the domain, including the airfoil and wind-tunnel walls. Solid and porous wall boundary conditions are implemented and tested for the domain boundaries representing the tunnel walls. Computations of the steady transonic aerodynamic characteristics show good agreement with the experimental results when a 50% porosity wall boundary condition is assumed for the wind-tunnel walls. Including the wall effects improved the agreement of the aeroelastic computations, which predicted limit-cycle flutter amplitudes in closer agreement with the experiment compared to the unbounded flow calculations.

Nomenclature

a_∞	=	freestream speed of sound
C_l	=	lift coefficient per unit span
C_m	=	pitching moment coefficient per unit span
C_p	=	pressure coefficient
c	=	chord length
D_h	=	plunge-damping coefficient
D_α	=	pitch-damping coefficient
f	=	frequency, Hz
h	=	plunge displacement (positive downward)
$\hat{h}$	=	maximum half amplitude of plunge
I_α	=	moment of inertia about x_p per unit span
K_h	=	spring constant for plunging
K_α	=	spring constant for pitching
k	=	reduced frequency, $\omega c/U_\infty$
k_h	=	reduced natural plunging frequency, $\omega_h c/U_\infty$
k_α	=	reduced natural pitching frequency, $\omega_\alpha c/U_\infty$
L	=	lift per unit span
M	=	pitching moment per unit span
M_∞	=	freestream Mach number
m	=	mass of the wing per unit span
Pr	=	Prandtl number
Re	=	Reynolds number
S_α	=	static moment, $x_\alpha m$
U_∞	=	freestream speed
u, w	=	Cartesian velocity components
x_p	=	leading edge to elastic axis distance
x_α	=	elastic axis to center of mass distance
$\dot{x}\|_{\text{wall}}$	=	velocity component of airfoil surface
$\dot{y}\|_{\text{wall}}$	=	velocity component of airfoil surface
α	=	angle of attack
α_0	=	spring-neutral angle of attack
$\bar{\alpha}$	=	average angle of incidence
$\hat{\alpha}$	=	maximum half amplitude of α
δ_h	=	nondimensional plunge-damping coefficient, $D_h/[2\sqrt{(m K_h)}]$
δ_α	=	nondimensional pitch-damping coefficient, $D_\alpha/[2\sqrt{(I_\alpha K_\alpha)}]$
Φ	=	phase angle between pitch and plunge
ω	=	circular frequency, $\omega = 2\pi f$
ω_h	=	undamped natural bending frequency, $\sqrt{(K_h/m)}$
ω_α	=	undamped natural torsional frequency, $\sqrt{(K_\alpha/I_\alpha)}$
$\cdot$	=	differentiation with respect to t
$'$	=	differentiation with respect to τ
c	=	corrected value

Received 2 December 2000; revision received 5 October 2001; accepted for publication 8 January 2002.

*Graduate Student, Department of Aeronautics and Astronautics. Student Member AIAA.
†Research Director, Institute of Applied and Computational Mathematics, P.O. Box 1527. Associate Fellow AIAA.
‡Professor, Department of Aeronautics and Astronautics. Fellow AIAA.

I. Introduction

THE understanding and prediction of transonic flutter is important for both aircraft wing and turbomachinery flows. The aerodynamic equations for transonic flow are nonlinear, and the development of aeroelastic solvers that can handle nonlinearities and take into account viscous flow effects is of great interest. Recently, numerical investigations of transonic flutter were performed by Weber et al.[1] The thin-layer Navier–Stokes equations were used for flowfield simulations of the experiment of Schewe and Deyhle[2] for a National Aerospace Laboratory (NLR) 7301 airfoil at $M_\infty = 0.768$. In these simulations, the effects of the wind-tunnel walls were accounted for by modifying the freestream speed and angle of incidence. It was found that it is necessary to model viscous effects and laminar–turbulent transition. A parametric study of turbulence modeling was performed using Baldwin–Lomax,[3] Baldwin–Barth,[4] and Spalart–Allmaras[5] models. The Spalart–Allmaras model yielded the best prediction for shock-induced separation and flutter characteristics. A very recent transition length model based on the work of Gostelow et al.[6] was also implemented, together with Michel's[7] transition onset criterion. It was found that the use of a transition model can improve numerical solutions for problems where the presence of separation bubbles, shock/boundary-layer interactions,

and/or the state of the boundary layer play an important role in the flow characteristics. Some improvement was obtained for steady-state solutions[1]; however, transition modeling did not affect flutter characteristics.

In the experiments,[2,8] a relatively large-size airfoil, compared with the test section dimensions, was used. In Ref. 1, the tunnel walls were not included. As a result, it was required to make corrections of the freestream speed, Mach number, and angle of attack in the simulations to obtain the experimentally measured pressure distributions. The best agreement with the experiment occurred when the angle of attack and the freestream Mach number were set to $\alpha_0 = -0.08$ deg and $M_\infty = 0.753$, respectively. The flutter calculations presented in Ref. 1 predicted the limit-cycle oscillations measured at DLR-Göttingen.[2,8] The frequency of oscillation and phase angle between the pitch and plunge motions were calculated quite accurately. However, the predicted flutter amplitude was found to be one order of magnitude larger than in the experiment.

In the experiments,[2,8] no attempt was made to correct the results for wind-tunnel interference effects. Therefore, a possible reason for the discrepancy between the computed[1] and measured[2,8] amplitudes of oscillation could be attributed to tunnel interference, even though steady-state corrections were applied for the computation. The importance of tunnel interference is well recognized,[9] but reliable quantitative estimates are still lacking. Recently, Khalid and Mokry[10] have presented Euler calculations for tunnel-wall interference effects in steady flow over a NACA 0012 airfoil in two-dimensional transonic flow. However, no Navier–Stokes studies seem to have been performed to analyze unsteady transonic interference effects. Therefore, the objective of the present work is to investigate numerically the influence of the wind-tunnel walls for both the steady and unsteady flow around the NLR 7301 airfoil.

The flow solver and the aeroelastic models used in the present investigation have been tested and validated extensively in previous studies for a variety of flow conditions. For example, the flow solver and the turbulence models have been tested for subsonic flow[11–13] and for transonic flow.[14] The aeroelastic model has been implemented and tested in Ref. 15 for inviscid flow calculations and in Refs. 1 and 16 for viscous transonic flow.

First, the ability of the multiblock version of the flow solver to predict accurately the flow over a stationary airfoil in a wind tunnel by including porous wall effects is demonstrated. Although the solver is capable of modeling transitional flow over the airfoil surface, this feature was not used because previous results of Ref. 1 have demonstrated only slight improvement. The effect of the assigned porosity for the wind-tunnel wall on the numerical solution is investigated. Numerical experiments for 25 and 50% porosity and varying porosity arrangements are carried out. The wall porosity that yields the best agreement with the experimental pressure distribution is identified. Next, numerical solutions are obtained for an airfoil free to oscillate in two degrees of freedom in transonic flow, and the results are compared with the measurements of Ref. 2.

II. Aerodynamics

The aeroelastic behavior of an airfoil can be predicted by solving the aerodynamic flow in combination with the structural dynamic response. The aerodynamic equations are presented first, and the method used to compute the structural response is presented in the next section.

A. Governing Equations

The time-dependent, compressible, two-dimensional, thin-layer Navier–Stokes equations in the strong conservation law form and curvilinear coordinate system (ξ, ζ) are used. These equations are

$$\partial_t \hat{\boldsymbol{Q}} + \partial_\xi \hat{\boldsymbol{F}} + \partial_\zeta \hat{\boldsymbol{G}} = Re^{-1} \partial_\zeta \hat{\boldsymbol{S}} \tag{1}$$

where $\hat{\boldsymbol{Q}}$ is the vector of conservative variables, $\hat{\boldsymbol{Q}} = (1/J)[\rho, \rho u, \rho w, e]^T$; $\hat{\boldsymbol{F}}$ and $\hat{\boldsymbol{G}}$ are the inviscid flux vectors, for example, $\hat{\boldsymbol{F}} = (1/J)[\rho U, \rho u U + \xi_x p, \rho w U + \xi_z p, (e+p)U - \xi_t p]^T$; and $\hat{\boldsymbol{S}}$ is the thin-layer approximation of the viscous fluxes in the ζ direction (normal to the airfoil surface). The terms U and W are the contravariant velocity components. The governing equations are nondimensionalized using c as the reference length, a_∞ as the reference speed, c/a_∞ as the reference time, ρ_∞ as the reference density, and $\rho_\infty a_\infty^2$ as the reference energy.

B. Numerical Method

The algorithm for numerical solution of these equations was developed and tested in Ref. 12. Oscillatory motion of the airfoil in the wind tunnel requires use of deforming grids. Therefore, modifications of the numerical algorithm according to the suggestions of Ref. 17 were incorporated to solve accurately the governing equations for flow problems that require temporal grid deformation. This algorithm is as follows:

$$\begin{aligned}
&\left[I(J^{-1})^{n+1} + h_\xi\left(\nabla_\xi \hat{A}^+_{i,k} + \Delta_\xi \hat{A}^-_{i,k}\right)\right]^p \left[I(J^{-1})^{n+1}\right. \\
&\qquad \left. + h_\zeta\left(\nabla_\zeta \hat{B}^+_{i,k} + \Delta_\zeta \hat{B}^-_{i,k} - Re^{-1}\delta_\zeta \hat{M}_{i,k}\right)\right]^p \left(\hat{Q}^{p+1}_{i,k} - \hat{Q}^p_{i,k}\right) \\
&= -\left[\left(\hat{Q}^p_{i,k} - \hat{Q}^n_{i,k}\right)(\Delta J^{-1}) + h_\xi\left(\hat{F}^p_{i+\frac{1}{2},k} - \hat{F}^p_{i-\frac{1}{2},k}\right)\right. \\
&\qquad \left. + h_\zeta\left(\hat{G}^p_{i,k+\frac{1}{2}} - \hat{G}^p_{i,k-\frac{1}{2}}\right) - Re^{-1} h_\zeta\left(\hat{S}^p_{i,k+\frac{1}{2}} - \hat{S}^p_{i,k-\frac{1}{2}}\right)\right]
\end{aligned} \tag{2}$$

In Eq. (2), $h_\xi = \Delta\tau/\Delta\xi$, etc., and $\hat{A}^\pm = \partial \hat{F}/\partial \hat{Q}$, etc., are the flux Jacobian matrices, and ∇, Δ, and δ are the forward, backward, and central difference operators, respectively. The quantities $\hat{F}_{i+1/2,k}$, $\hat{G}_{i,k+1/2}$, and $\hat{S}_{i,k+1/2}$ are numerical fluxes. The superscript n denotes the physical time step, and the superscript p refers to Newton subiterations within each physical time step. J^{n+1} is the Jacobian of the transformation of the deformed grid at the $n+1$ time step, and $\Delta J^{-1} = -\Delta\tau[(\xi_t)^{n+1}_\xi + (\zeta_t)^{n+1}_\zeta]$.

The inviscid fluxes, $\hat{F}$ and $\hat{G}$, are evaluated by means of Osher's third-order accurate, upwind-biased scheme.[18,19] Linearization of the left-hand side of Eq. (2) is performed by evaluating the flux Jacobian matrices, A and B, with the Steger–Warming flux-vector splitting.[20] The viscous fluxes are computed with second-order central differences. Furthermore, a standard minmod total variation diminishing flux limiter[18] is used to eliminate numerical oscillations at shocks developed at transonic Mach numbers.

Time accuracy is improved by performing Newton subiterations to convergence within each physical step. These subiterations minimize the linearization and factorization errors and help drive the left-hand side of Eq. (2) to zero. Numerical experiments have shown that larger Courant–Friedrichs–Lewy numbers, that is, a larger time step, could be used if the number of Newton iterations was increased. The optimal efficiency depends on the grid density and flow conditions, but the best computational performance appears to occur by using four to five subiterations on coarse grids (inviscid flow simulations) and two to three subiterations on fine grids (Navier–Stokes simulations).

The turbulence modeling is based either on the standard algebraic model of Baldwin and Lomax[3] or one-equation models of Baldwin and Barth[4] or Spalart and Allmaras[5] (SA). The eddy viscosity obtained from the models is used for the computation of the fully turbulent region. The present simulations were performed with the SA model.

C. Three-Block Grid

The geometry of a wind-tunnel test section involves a mesh that is very long in the streamwise direction compared to its height. Construction of a single-block grid implies a very skewed grid and use of an excessive amount of grid points in regions far from the airfoil. Furthermore, it would not be possible to maintain grid orthogonality close to the walls using a single-block grid. These problems can be minimized by using a three-block grid (Fig. 1), where the governing equations are solved in each block separately.

The first block 1 is a C-type grid and contains the airfoil and the wind-tunnel walls above and below it. The grid spacing in the normal direction close to the grid boundaries representing the tunnel walls in block 1 is appropriate only for inviscid computations. The second and third grid blocks are Cartesian-type inviscid grids and model the upstream and downstream portions of the wind tunnel, respectively.

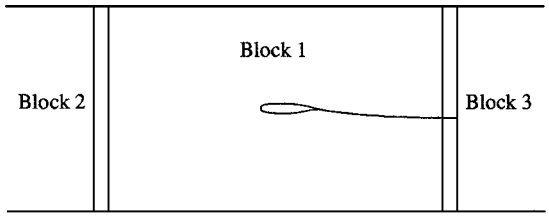

Fig. 1 Schematic of the three-block grid, inviscid tunnel walls.

These blocks have a narrow but finite region of overlapping with the first grid block. Data transfer between the inflow block 2, outflow block 3, and main block 1 is obtained by trilinear interpolation of the conservative variables (ρ, ρu, ρw, e). Figure 1 shows the three-block grid concept adopted in this work. One can see the regions of overlapping between blocks 1 and 2 as well as blocks 1 and 3.

D. Boundary Conditions

For inviscid flow solutions, the viscous terms on the right-hand side of Eq. (1) are set to zero, and flow-tangency boundary conditions are used at the surface. For Navier–Stokes solutions, the no-slip condition is applied. Density and pressure are extrapolated to the wall for both Euler and Navier–Stokes solutions.

For unsteady airfoil motions, the flow-tangency and no-slip conditions are modified to include the local motion of the surface, which also contributes to the pressure on the surface. Therefore, the following momentum equation normal to the surface (ζ direction) is solved to compute the pressure more accurately:

$$\partial_\zeta p|_{\text{wall}} = -\frac{1}{\nabla^2 \zeta}\left[\rho\, \partial_t \begin{Bmatrix} \dot{x}|_{\text{wall}} \\ \dot{y}|_{\text{wall}} \end{Bmatrix} \cdot \nabla\zeta + \partial_\zeta \rho|_{\text{wall}} \nabla\xi \cdot \nabla\zeta\right] \quad (3)$$

where $\dot{x}|_{\text{wall}}$ and $\dot{y}|_{\text{wall}}$ are the components of the airfoil velocity. Furthermore, if it is assumed that the grid is orthogonal at the surface, $\nabla\xi \cdot \nabla\zeta = 0$. If the airfoil is stationary, the normal pressure gradient vanishes in agreement with boundary-layer theory.

The flow through wind-tunnel section blocks 2 and 3 is assumed inviscid, and the Euler equations are solved in these domains. The upper and lower boundaries in sections 2 and 3, which represent tunnel walls, are assumed solid, and the usual flow-tangency condition is applied. Two types of inviscid flow boundary conditions are implemented for the wind-tunnel walls, above and below the airfoil, in block 1. For solid tunnel walls, the flow-tangency condition is imposed. The second boundary condition considers the tunnel wall as porous. This is implemented by treating certain parts of the domain boundary by inviscid wall boundary conditions and the remaining portion as outflow through holes. The values of the flow variables in a hole region are extrapolated from their values at the interior cells. The grid is constructed with an approximately constant grid spacing in the streamwise direction for the boundary, which represents the wall so that a rate of porosity of 25%, for instance, can be modeled by considering three grid cells as a solid wall and one grid cell as a hole.

Inflow and outflow boundary conditions are imposed on the upstream boundary of block 2 and the downstream boundary of block 3, respectively. For the inflow boundary, flow properties such as pressure, temperature, and velocity are specified whereas the density is extrapolated from the neighbor interior points. Static pressure is specified for the outflow boundary condition and all other properties are extrapolated from the interior. The other boundaries on the right and on the left of domains 2 and 3, respectively, are updated by trilinear interpolation from domain 1.

E. Grid Motion

The objective of this investigation is the simulation of an oscillatory airfoil motion inside a wind tunnel. An additional problem arises for the adjustment of the grid due to the motion of the airfoil. The wind-tunnel walls are fixed at all times while the airfoil is moving; therefore, the grid must deform in time to accommodate the relative motion between the airfoil and the walls.

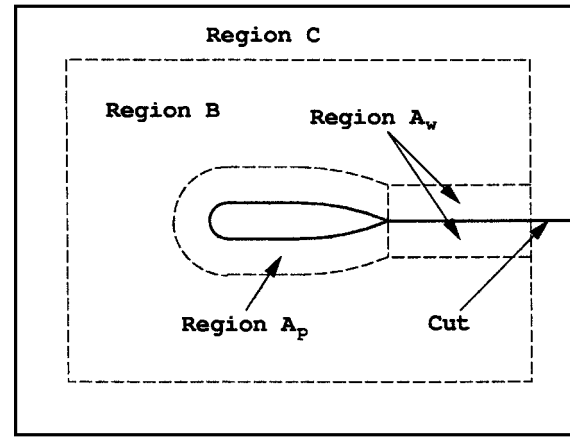

Fig. 2 Schematic of the regions for grid motion.

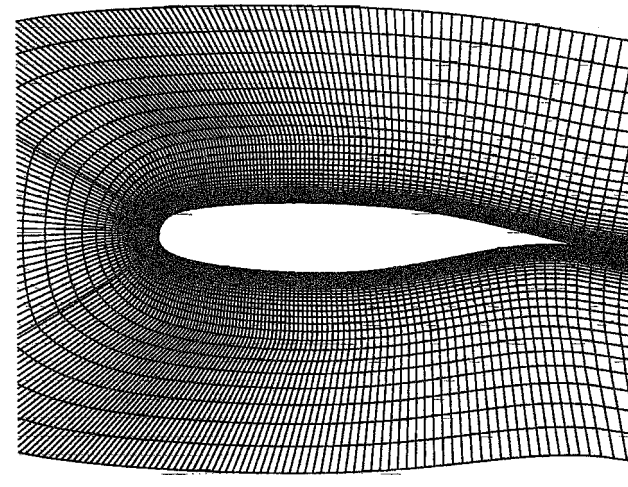

Fig. 3 View of the C-type grid in the vicinity of the NLR 7301 airfoil.

The change in the grid is treated by dividing the whole domain of the C-type grid around the airfoil into four regions. Figure 2 shows how these regions are distributed along the the main block. The first region is called A_p and corresponds to the portion of the block that is close to the surface of the airfoil and used to capture the viscous flow effects. In this region, the mesh does not deform but simply rotates and translates following the same rotation and translation of the airfoil. This means that there is no volumetric change of the grid cells in the region A_p at all times. Another partition of the grid, denoted C, is the one including the proximity of the wind-tunnel walls, and portions of the blocks 2 and 3 overlap sections. This region also remains fixed at all times, and, therefore, the grid points do not change in time for an observer sitting on the wind-tunnel walls.

The region A_w corresponds to the wake following region A_p. It is adjusted to the movement of the airfoil. The adjustment is done using an algebraic grid generator that redistributes the grid points. Linear interpolation for the grid points along a constant ζ line is applied. This procedure takes into account that the displacement of a grid point in the region A_w is proportional to the relative displacement of the corresponding points (same ζ coordinate) in regions A_p and C. Finally, whereas the relative location of regions A_w and A_p with respect to the tunnel walls change, region B (where the grid deformation is the largest) is adjusted to provide a smooth grid between regions A and C. This adjustment, again, is done by means of the algebraic grid generator. However, this time, linear interpolation is performed along constant ξ lines. An example of a deformed grid is shown in Fig. 3. This grid is obtained by rotating an initial grid from $\alpha = 0$ deg to the angle of incidence $\alpha = 1.28$ deg.

III. Structural Dynamics

Structural modeling is facilitated using a two-degree-of-freedom spring/mass/damper system (Fig. 4) to simulate the bending and twisting of a wing.

A. Governing Equations

The equations governing this motion are

$$m\ddot{h} - S_\alpha \ddot{\alpha} + D_h \dot{h} + m\omega_h^2 h = L \tag{4}$$

$$-S_\alpha \ddot{h} + I_\alpha \ddot{\alpha} + D_\alpha \dot{\alpha} + I_\alpha \omega_\alpha^2 (\alpha - \alpha_0) = M \tag{5}$$

where the dots denote differentiation with respect to time.

Equations (4) and (5) are nondimensionalized using reference length c, reference velocity a_∞, reference mass $\rho_\infty \pi (c/2)^2$, and reference inertia $\rho_\infty \pi (c/2)^2 c^2$. Rewriting Eqs. (4) and (5) in matrix notation, one obtains

$$[\boldsymbol{M}]\{X\}'' + [\boldsymbol{D}]\{X\}' + [\boldsymbol{K}]\{X\} = \{F\} \tag{6}$$

where

$$[\boldsymbol{M}] = \begin{bmatrix} m & -S_\alpha \\ -S_\alpha & I_\alpha \end{bmatrix}, \qquad [\boldsymbol{D}] = \begin{bmatrix} 2\delta_h m k_h & 0 \\ 0 & 2\delta_\alpha I_\alpha k_\alpha \end{bmatrix}$$

$$[\boldsymbol{K}] = \begin{bmatrix} m k_h^2 & 0 \\ 0 & I_\alpha k_\alpha^2 \end{bmatrix}, \qquad \{X\} = \begin{Bmatrix} h \\ \alpha - \alpha_0 \end{Bmatrix}$$

$$\{F\} = \frac{2}{\pi} M_\infty^2 \begin{Bmatrix} C_l \\ C_m \end{Bmatrix}$$

The primes denote differentiation with respect to dimensionless time, $\tau = t a_\infty / c$, and the other parameters, that is, m, $I_\alpha, \ldots$, are now nondimensional. Note that k_h and k_α, appearing in the matrices $[\boldsymbol{K}]$ and $[\boldsymbol{D}]$, are reduced natural frequencies based on the freestream speed of sound, as opposed to the conventional form as presented in the Nomenclature. However, in the interest of clarity, presented results utilize the conventional definition, based on freestream velocity.

B. Numerical Method

Equation (6) is a system of two coupled second-order, ordinary differential equations. Coupling is obtained through the terms containing S_α and the dependence of C_l and C_m on h and α. The system is nonlinear through the nonlinearity of C_l and C_m. Linearization is introduced by treating C_l and C_m as constants, computed from the earlier time step of the flow solution.

Simulations with a single degree of freedom may be performed by setting $S_\alpha = 0$ and either $m = \infty$ and $\omega_h = 0$ or $I_\alpha = \infty$ and $\omega_\alpha = 0$ for pitching-only or plunging-only motions, respectively.

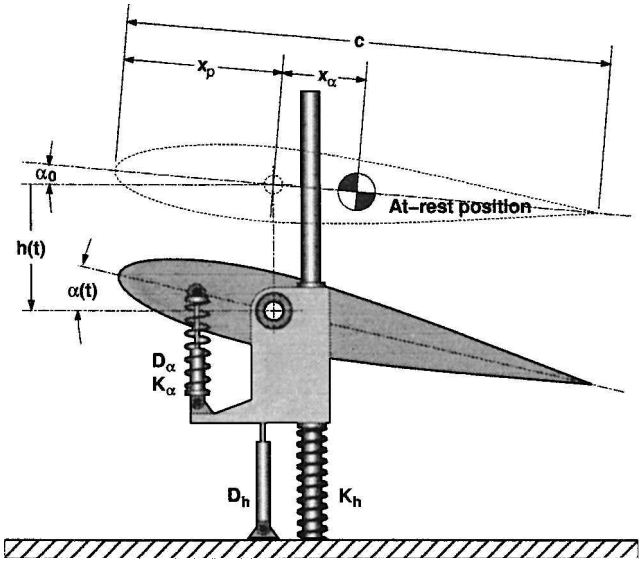

Fig. 4 Schematic of the spring/mass/damper system.

Equation (6) is advanced in time by inverting the system, yielding

$$\{X\}'' = [\boldsymbol{M}]^{-1}\{F\} - [\boldsymbol{M}]^{-1}[\boldsymbol{K}]\{X\} - [\boldsymbol{M}]^{-1}[\boldsymbol{D}]\{X\}' \tag{7}$$

then rewriting the result as a system of two coupled first-order equations

$$\{X\}' = \{Y\}$$

$$\{Y\}' = [\boldsymbol{M}]^{-1}\{F\} - [\boldsymbol{M}]^{-1}[\boldsymbol{K}]\{X\} - [\boldsymbol{M}]^{-1}[\boldsymbol{D}]\{Y\} \tag{8}$$

Finally, time integration is performed using a first-order accurate explicit Euler scheme. In Ref. 1, it was found that use of higher-order methods to solve the structural dynamics equations did not improve the solution quality because the time steps required for the stability of the Navier–Stokes equations yield very high resolution in time for Eq. (6).

IV. Results

There are several factors that may affect transonic flow and flutter in the wind tunnel. It appears that wall porosity has the most pronounced effect. Therefore, the approach adopted during this work was based on the determination of a porosity that yields a steady-state surface pressure distribution for the NLR 7301 airfoil, in the presence of the wind-tunnel walls, which is in agreement with the experiment. Once a satisfactory porosity ratio was determined, the flutter computations were performed. Adjustment of other flow parameters of the experiment, such as inflow and outflow boundary conditions, was not attempted. The wind-tunnel steady flow test was performed at a Mach number of $M_\infty = 0.768$ and an angle of attack of $\alpha_0 = 1.28$ deg. These flow conditions are used in the present simulation. In the previous investigations of Ref. 1, where wind-tunnel walls were not included, it was necessary to modify both the angle of attack and the Mach number in the simulations to obtain agreement with the experiment.

The experiments were conducted at the DLR-Göttingen wind tunnel. The wind tunnel height to airfoil chord ratio was $H/c = 3.3333$. The open area ratio, defined as the area of the holes divided by the total area of the wall, was stated as $A_{\text{holes}}/A_{\text{wall}} = 0.06$ and the porosity parameter associated with the walls as $\delta = 0.25$.

A systematic investigation of the influence of the wind-tunnel walls on the surface pressure distribution of the profile was carried out. It was found that the tunnel-wall porosity has a dramatic effect on the airfoil surface and field pressure distributions. Based on the observation that the presence and geometry of the walls have a much stronger influence on the results, rather than transition, calculations with transition were not attempted for this particular problem. The results for the steady calculations were used, then, as the start for the unsteady simulations. In the previous work conducted in Ref. 1, the neutral spring angle was modified to account for the wind-tunnel interference. In the present work, however, for the reasons discussed earlier, the exact same values of the wind-tunnel test conditions were used.

All steady-state and unsteady computations were carried out on a C-type 221×91 point main block grid 1, shown in Fig. 3, which was generated from the original NLR 7301 airfoil surface data. Blocks 2 and 3 were Cartesian type and contain 45×61 points along the streamwise and normal directions, respectively. No grid-sensitivity investigation was performed in this study because the results of Ref. 1 showed that numerical solutions obtained with a 221×91 point grid and a $y^+ \leq 1.0$ were as accurate as the results computed on higher-density grids. The SA turbulence model was used in all computations based on the conclusion of Weber et al.[1] that it allowed the largest time step.

All of the computations were performed as time accurate using a constant time step. For fixed angles of incidence, the solution was run for a long time after convergence of loads was achieved to ensure that all flow disturbances from the initial transients were swept off of the domain and a full communication between inflow and outflow boundaries was established. Steady-state solutions were run until a nondimensional time 500. Therefore, the computational domain was swept out for more than 20 times. At convergence, all solutions at fixed angles of incidence exhibited no unsteadiness.

A. Steady-State Computations

The first step in the course of this study was the computation of a steady-state flow around the NLR 7301 airfoil at $\alpha_0 = 1.28$ deg, $M_\infty = 0.768$, and $Re_c = 1.727 \times 10^6$, without the presence of the wind tunnel. This was done to establish a basis for comparison with the computations considering the interference of the wind-tunnel walls.

A first attempt to model the wind-tunnel interference was done by considering the walls as being completely solid. The results are shown in Fig. 5. Poor agreement with the experimental data was obtained. The pressure coefficients at the leading and trailing edges were not in agreement with the measurements, and the position of the shock on both pressure and suction sides was not predicted correctly. Although the values for the pressure distribution were not close to the measurements, the tendency of the solution to move toward the experimental values, when the walls were taken into account, was evident. This was the motivation to move on and treat the porosity wall boundary conditions more carefully.

A transonic wind-tunnel test section usually has perforated walls. The holes are inclined with respect to the wall and are introduced to minimize reflections. It is, however, very difficult to model a geometry involving flow curvature in a two-dimensional solution. Despite that, and taking advantage of a reasonably constant grid spacing along the walls, a 50% porosity was imposed, considering one cell as being solid and the next one as being a hole (referred to, from now on, as 50% arrangement 1-1 arrangement).

The results for a 50% 1-1 porous wall arrangement did not differ too much from the ones obtained for a solid wall. A comparison with the experimental data and free-flight condition is presented in Fig. 6. Although these results still differed from the measurements

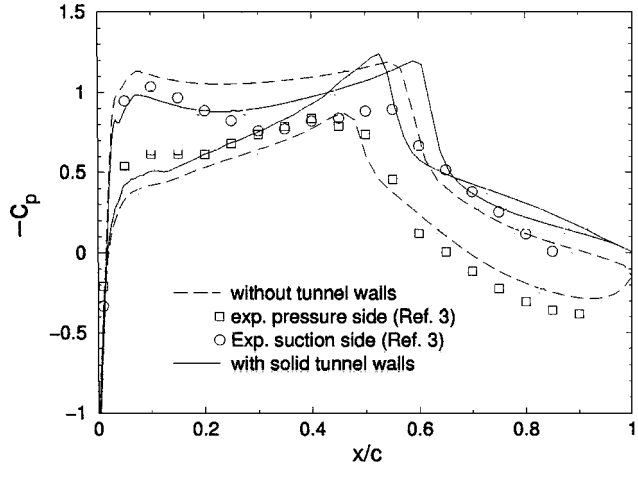

Fig. 5 Comparison of surface pressure coefficient; $M_\infty = 0.768$ and $\alpha_0 = 1.28$ deg.

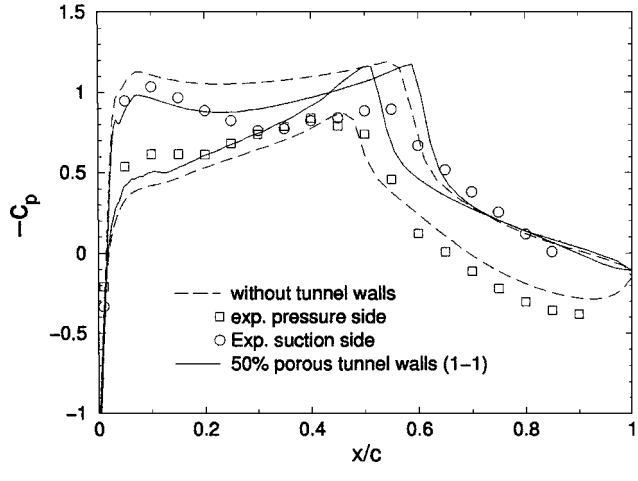

Fig. 6 Comparison of surface pressure coefficient for tunnel wall with 50% porosity 1-1 arrangement; $M_\infty = 0.768$ and $\alpha_0 = 1.28$ deg.

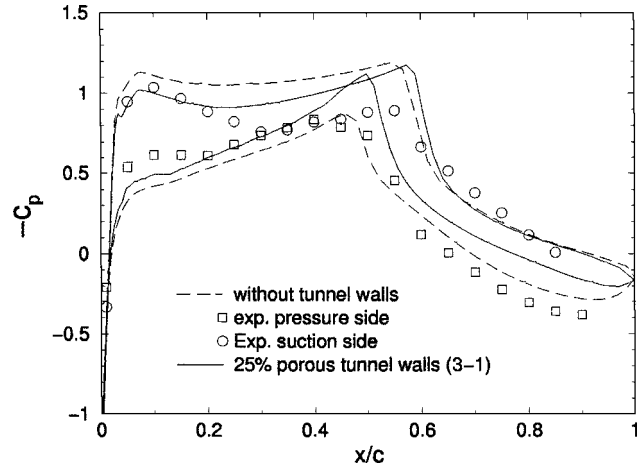

Fig. 7 Comparison of surface pressure coefficient for tunnel wall with 25% porosity 3-1 arrangement; $M_\infty = 0.768$ and $\alpha_0 = 1.28$ deg.

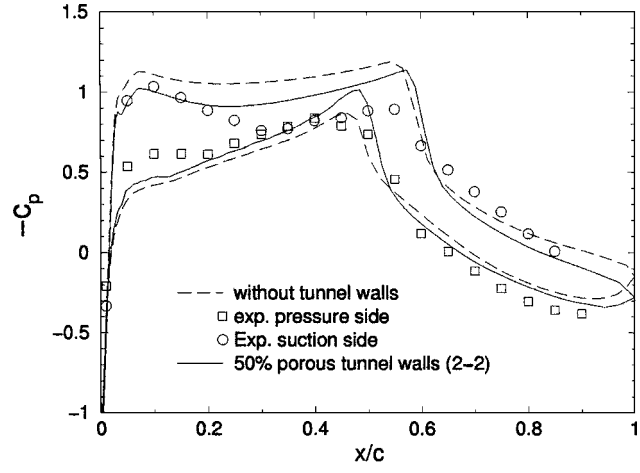

Fig. 8 Comparison of surface pressure coefficient for tunnel wall with 50% porosity 2-2 arrangement; $M_\infty = 0.768$ and $\alpha_0 = 1.28$ deg.

in the wind tunnel, they showed an improvement compared to the results obtained for the solid wall. Therefore, a 25% porosity arrangement 3-1, with three solid and one hole cell, was implemented next. Figure 7 shows the results for the 25% case 3-1. These results show further improvement compared to the 50% case 1-1.

A 50% porosity, which is believed to approximate more closely the porosity in the three-dimensional wind tunnel, can be modeled by several combinations of cells being considered as solid and holes, for example, arrangements 1-1, 2-2, 3-3, etc. An optimum arrangement for a certain value of porosity may exist. To find the best arrangement for 50% porosity, trials with settings 2-2, 3-3, and 4-4 were attempted and the results are presented in Figs. 8, 9, and 10, respectively. It can be seen that the porosity arrangement 4-4 yielded the best agreement with the experimental results. In particular, the position of the shocks on both suction and pressure side was predicted fairly accurately.

There is a slight difference between the pressure distribution for the cases 2-2 and 4-4. For instance, the location of the shock on the suction side of the airfoil is better predicted for arrangement 4-4. The numerical solution predicted flow going out, through the wall boundary cells modeled as holes, for the upstream portion of the test section. Because of conservation of mass, there is also flow going back to the test section, mainly through the downstream part of the upper wall. A larger amount of inflow is obtained for the arrangement 4-4 than it is for arrangement 2-2, as shown in Figs. 11 and 12. The effect of this incoming flow through the holes is to induce a displacement on the streamlines, narrowing the distance across the test section available for the main flow. This behavior altered the structure of the flowfield in the vicinity of the tunnel wall with the incoming flow and affected the position of the shock at the suction side of the airfoil. Figures 11 and 12 show the Mach contour

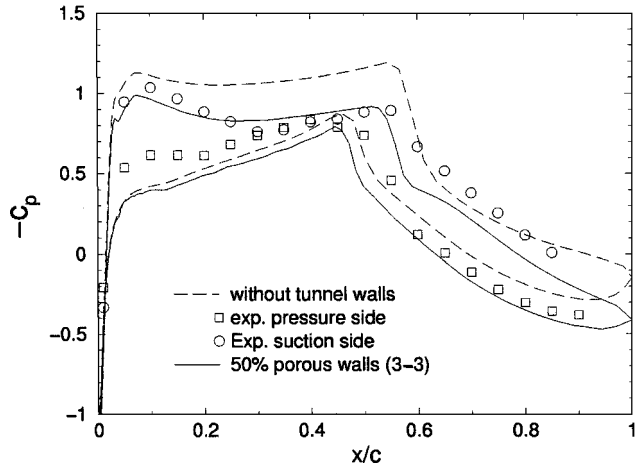

Fig. 9 Comparison of surface pressure coefficient for tunnel wall with 50% porosity 3-3 arrangement; $M_\infty = 0.768$ and $\alpha_0 = 1.28$ deg.

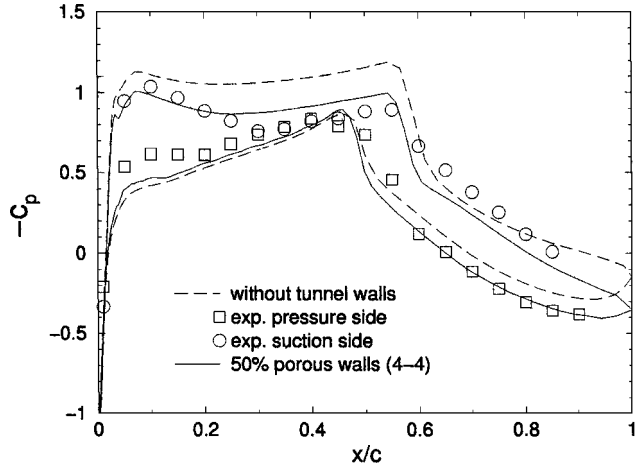

Fig. 10 Comparison of surface pressure coefficient for tunnel wall with 50% porosity 4-4 arrangement; $M_\infty = 0.768$ and $\alpha_0 = 1.28$ deg.

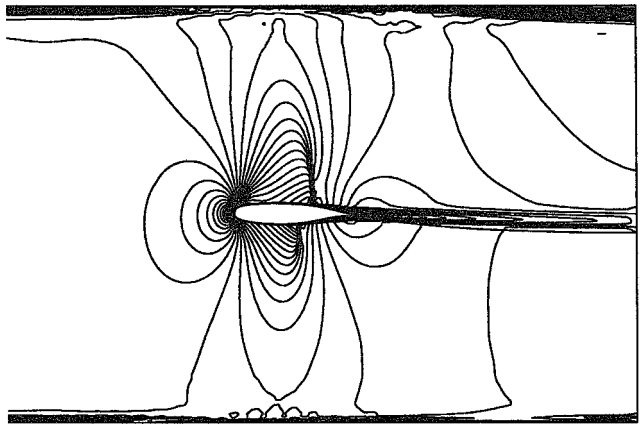

Fig. 11 Mach contour lines; 50% porosity 2-2 arrangement; $M_\infty = 0.768$ and $\alpha_0 = 1.28$ deg.

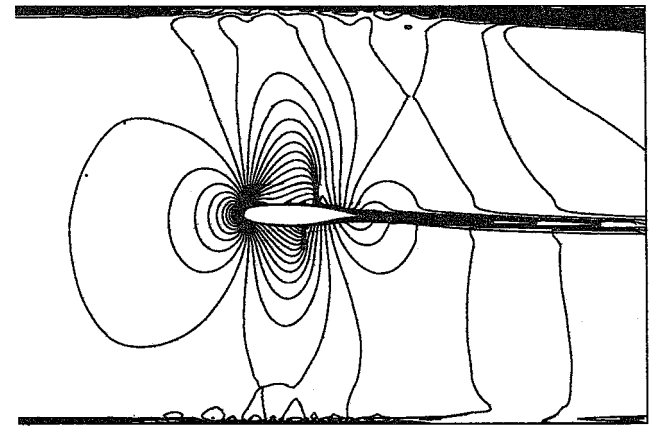

Fig. 12 Mach contour lines, 50% porosity 4-4 arrangement; $M_\infty = 0.768$ and $\alpha_0 = 1.28$ deg.

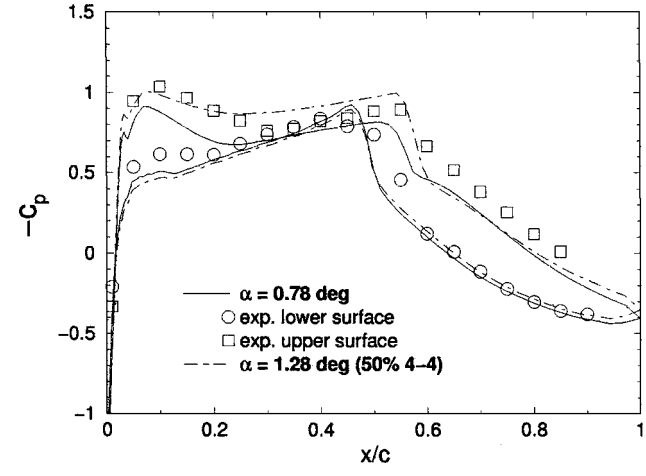

Fig. 13 Comparison of surface pressure coefficient for tunnel wall with 50% 4-4 porosity; $M_\infty = 0.768$ and $\alpha_0 = 0.78$ deg.

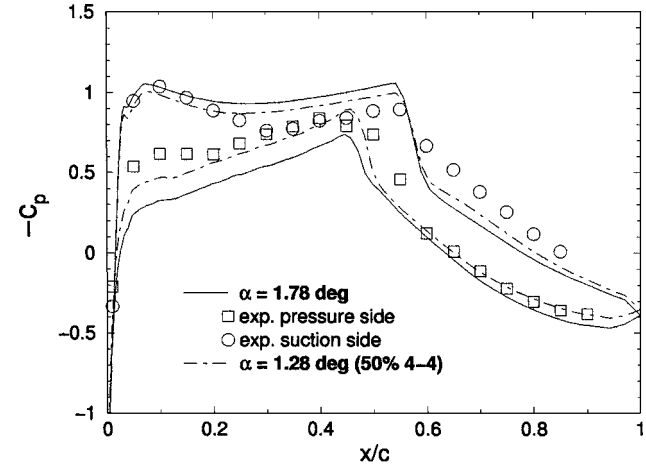

Fig. 14 Comparison of surface pressure coefficient for tunnel wall with 50% 4-4 porosity; $M_\infty = 0.768$ and $\alpha_0 = 1.78$ deg.

lines for the cases 2-2 and 4-4, respectively, where the difference in the flowfield for these two arrangements is evident.

The main conclusion, as far as the steady-state computations are concerned, is that the wind-tunnel walls have a very strong influence on the computed flowfield around the NLR 7301 airfoil. This confirms the procedure adopted in the previous work of Weber et al.[1] to correct the nominal values of flow parameters used in the test to account for the wind-tunnel interference. It can also be concluded that the computed flow through the holes of the wall boundaries has a considerable influence on the results. This means that a better agreement with the experiment requires a better prediction of the flow in this region. However, this is questionable in a two-dimensional calculation. In addition, other inflow and outflow tunnel conditions may have an effect on the computed solutions.

Some calculations for different angles of attack were also performed to further investigate if the best results were obtained by imposing the nominal wind-tunnel test conditions. Simulations for an angle $\alpha_0 = 0.78$ deg, smaller than the experiment, and $\alpha_0 = 1.78$ deg, larger than the experiment, are shown in Figs. 13 and 14, respectively, for a 50% porous wall arrangement 4-4. This shows

that, indeed, the best agreement with the experimental results was achieved by the nominal conditions of the test.

B. Flutter Computations

Based on the results for the steady computations, the flutter simulations were performed using a 50% porous arrangement 4-4 for the wind-tunnel wall boundary condition. The nominal conditions of the wind-tunnel test were preserved, namely, $M_\infty = 0.768$, $\alpha_0 = 1.28$ deg, and $Re_c = 1.727 \times 10^6$, as well as the spring-neutral angle of attack. Note that this value was also modified in Ref. 1 to account for wind-tunnel interference, as shown in Table 1. The rest of the boundary conditions was specified as stated in Sec. II.D. All time-accurate flutter computations were performed assuming fully turbulent flow. The SA turbulence model was used. Three Newton subiterations were used in all time-accurate unsteady calculations. The computations predicted flutter in two degrees of freedom. Limit-cycle oscillations were computed in agreement with the wind-tunnel test. Figure 15 shows the time history of the pitching amplitude that was obtained from the computations. Unsteady solutions were obtained using an Athlon-1-GHz personal computer. The typical run time for this machine was approximately 0.000133 s/iteration/grid point.

In the experimental test case,[2] limit-cycle oscillations in pitch and plunge were observed. The experiment was conducted at a total pressure of 0.45 bar and a dynamic pressure of 0.126 bar. A time-averaged angle of attack of $\bar{\alpha} = 1.28$ deg was measured for an angle of attack at a wind-off condition of $\alpha_0 = 1.91$ deg, which is equivalent to the spring-neutral angle of attack α_0 in the numerical simulation. The dimensionless structural parameters of the experiment are summarized in Table 2. The same parameters are used for the aeroelastic computation.

The results of the flutter computation are given in detail in Table 3. The freestream Mach number M_∞, angle of attack α_c, and spring-neutral angle of attack α_{0c} are given in Table 1. For comparison, the values of the experiment are given in the first row of Table 1. The values used in the computations for the present work and for Ref. 1 are given in the second and third rows, respectively. Flutter frequency, phase, amplitudes $\hat{\alpha}$ and $\hat{h}$, and mean angle of attack $\bar{\alpha}$ are shown in Table 3.

The results of the present work show better agreement with the experiment than the values obtained in Ref. 1, for the parameters $\bar{\alpha}$, $\hat{\alpha}$, and $\hat{h}$. The average incidence angle $\bar{\alpha}$ was predicted within an error of 3%. The values of computed amplitudes $\hat{\alpha}$ and $\hat{h}$, although still different from the experiment, were much better than the ones predicted previously in Ref. 1. This confirms one of the possible reasons for the discrepancy between measured and computed amplitudes, pointed out by Weber et al.,[1] related to the omission of unsteady wind-tunnel interference effects. Taking into account that the assigned porosity did not yield a perfect agreement between the experimental and computed surface pressure distribution (Fig. 10) and that additional uncertainty factors may exist, we conclude that a significant improvement has been obtained.

Table 1 Initial values of the computations

Method	M_∞	α_c, deg	α_{0c}, deg
Experiment[a]	0.768	1.28	1.91
SA[b]	0.768	1.28	1.91
SA[c]	0.753	−0.08	0.635

[a]Without wind-tunnel corrections.
[b]With 50% (4-4) porous wall.
[c]Ref. 1; fully turbulent (221 × 91 point grid).

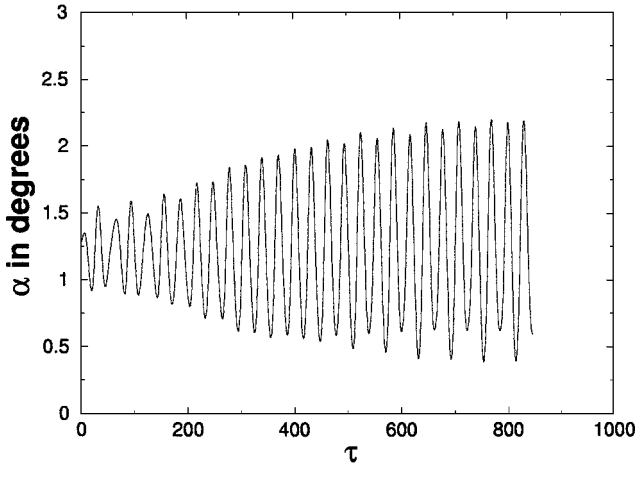

Fig. 15 Computed variation of the incidence angle for transonic flutter at $M_\infty = 0.768$.

Table 2 Structural parameters

Parameter	Value
x_p	0.2500
x_α	0.0485
m	992.00
I_α	35.600
k_α	0.3280
k_h	0.2510
δ_α	0.0041
δ_h	0.0073

Table 3 Flutter results

Method	$\bar{\alpha}$, deg	$\hat{\alpha}$, deg	$\hat{h}$, mm	f, Hz	Φ, deg
Experiment[a]	1.28	0.18	0.65	32.85	176.7
SA[b]	1.24	0.78	2.9	36.7	149
SA[c]	0.07	3.78	11.1	32.30	171.8

[a]Without wind-tunnel corrections.
[b]With 50% (4-4) porous wall.
[c]Ref. 1; fully turbulent (221 × 91 point grid).

Flutter frequency and intermodal phase angle were predicted less closely in the present study. The error for the flutter frequency was around 12%, but, for the intermodal phase angle, it reached values as high as 16%. These parameters were predicted more closely in Ref. 1. The values of frequencies, amplitudes, and phase angles were calculated by means of a discrete Fourier transform analysis of the last 10 cycles. The large discrepancy observed on the computed intermodal phase angle Φ could be attributed to the extremely low amplitude of the predicted plunge displacement $\hat{h}$. Therefore, a small error in the computation of the incidence angle can shift quite significantly the relative position of these two curves and, thus, induce a considerable error in the prediction of the intermodal phase angle. The error in the prediction of the flutter frequency could also be attributed to an insufficient resolution of the unsteady flow through the slots of the wind-tunnel walls. As happened for the steady-state study, the computed unsteady flow through the holes of the tunnel wall boundary could have a significant effect on the flowfield around the airfoil.

V. Conclusions

Progress was achieved with the present work because the nominal test conditions were used in all calculations. There was no need to adjust any parameter to get a better agreement with the experiment. In fact, when a parametric variation of the angle of attack was attempted, the agreement with the experimental values deteriorated compared to the results for the nominal angle of attack. The modeling of the tunnel wall porosity was found to affect significantly the numerical predictions of the steady-state characteristics. The arrangement used to describe a particular value of porosity for the wall boundary condition is also important in the computations. The numerical simulations predicted suction into the tunnel in the downstream portion of the upper wall of the test section. Although the presence of this flow through the wall boundary holes had a beneficial effect on the computed steady-state pressure distribution, this behavior should be further investigated.

The transonic two-degree-of-freedom bending/torsion flutter analysis of the NLR 7301 supercritical airfoil section, in a wind tunnel that was modeled by a 50% porosity, yielded a significantly improved prediction of the flutter amplitudes compared to the values

found in Ref. 1 based on unbounded flow computations. However, the computed phase angle between the pitch and plunge motions was smaller, and the flutter frequency was larger, than found in the experiment. This discrepancy may be caused by the modeling of the wind-tunnel wall interference using inviscid flow assumptions. Further work to assess fully the adequacy of this assumption and to study effects of wall porosity on flutter characteristics is currently underway.[16]

Acknowledgments

The first author is grateful to Stefan Weber for all of his support during this work, as well as to Kevin Jones of the Naval Postgraduate School for valuable suggestions about moving the grid.

References

[1]Weber, S., Jones, K. D., Ekaterinaris, J. A., and Platzer, M. F., "Transonic Flutter Computations for a Two-Dimensional Supercritical Wing," AIAA Paper 99-0798, 1999.

[2]Schewe, G., and Deyhle, H., "Experiments on Transonic Flutter of a Two-Dimensional Supercritical Wing with Emphasis on Non-Linear Effects," *Proceedings of the Royal Aeronautical Society Conference on Unsteady Aerodynamics*, London, July 1996.

[3]Baldwin, B. S., and Lomax, H., "Thin-Layer Approximation and Algebraic Model for Separated Turbulent Flow," AIAA Paper 78-257, 1978.

[4]Baldwin, B. S., and Barth, T. J., "A One-Equation Turbulence Transport Model for High Reynolds Number Wall-Bounded Flows," NASA TM 102847, 1990.

[5]Spalart, P. R., and Allmaras, S. R., "One-Equation Turbulence Model for Aerodynamic Flows," AIAA Paper 92-0439, 1992.

[6]Gostelow, J. P., Melwani, N., and Walker, G. J., "Effects of a Streamwise Pressure Gradient on Turbulent Spot Development," *Journal of Turbomachinery*, Vol. 118, No. 4, 1996, pp. 737–747.

[7]Michel, R., "Etude de la Transition sur les Profiles d'Aile," ONERA, Rept. 1/1578A, 1957.

[8]Knipfer, A., Schewe, G., and Wendt, V., "Numerische und experimentelle Untersuchungen an einem schwingenden NLR7301-Profil in transsonischer Stroemung, Teil 1: Flattern und erzwungene Schwingungen," DLR Bericht IB 232-98 J 05, 1998.

[9]Mokry, M., Chan, Y. Y., and Jones, D. J., "Two-Dimensional Wind Tunnel Wall Interference," AGARDograph 281, Nov. 1983.

[10]Khalid, M., and Mokry, M., "NPARC Study of a Two-Dimensional Transonic Wall Interference," *Journal of Aircraft*, Vol. 33, No. 5, 1996, pp. 906–912.

[11]Sanz, W., and Platzer, M. F., "On the Navier–Stokes Calculation of Separation Bubbles with a New Transition Model," *Journal of Turbomachinery*, Vol. 120, No. 1, 1998, pp. 36–42.

[12]Ekaterinaris, J. A., and Menter, F. R., "Computation of Oscillating Airfoil Flows with One- and Two-Equation Turbulence Models," *AIAA Journal*, Vol. 32, No. 12, 1994, pp. 2359–2365.

[13]Ekaterinaris, J. A., Sorensen, N. N., and Rasmussen, F., "Numerical Investigation of Airfoil Dynamic Stall in Simultaneous Harmonic Oscillatory and Translatory Motion," *Journal of Solar Energy Engineering*, Vol. 120, No. 2, 1998, pp. 75–83.

[14]Ekaterinaris, J. A., Cricelli, A. S., and Platzer, M. F., "A Zonal Method for Unsteady, Viscous, Compressible Airfoil Flows," *Journal of Fluids and Structures*, Vol. 8, No. 2, 1994, pp. 107–123.

[15]Jones, K. D., and Platzer, M. F., "Airfoil Geometry and Flow Compressibility Effects on Wing and Blade Flutter," AIAA Paper 98-0517, 1998.

[16]Castro, B. M., Weber, S., Jones, K. D., Platzer, M. F., and Ekaterinaris, J. A., "Analysis of the Effect of Porous Wall Interference on Transonic Airfoil Flutter," AIAA Paper 2001-2725, 2001.

[17]Thomas, P. D., and Lombard, C. K., "Geometric Conservation Law and Its Applications to Flow Computations on Moving Grids," *AIAA Journal*, Vol. 17, No. 10, 1979, pp. 1030–1037.

[18]Osher, S., and Chakravarthy, S. R., "New Class of High-Accuracy Total Variation Diminishing Schemes for Hyperbolic Conservation Laws," AIAA Paper 85-0363, 1985.

[19]Chakravarthy, S. R., and Osher, S., "Numerical Experiments with the Osher Upwind Scheme for the Euler Equations," *AIAA Journal*, Vol. 21, No. 11, 1983, pp. 1241–1248.

[20]Steger, J. L., and Warming, R. F., "Flux Vector Splitting of the Inviscid Gas Dynamic Equations with Applications to Finite-Difference Methods," *Journal of Computational Physics*, Vol. 40, No. 2, 1981, pp. 263–293.

E. Livne
Associate Editor